$CaCO_3$ Fouling on Microscale–Nanoscale Hydrophobic Titania–Fluoroalkylsilane Films in Pool Boiling

Yongwei Cai
Dept. of Chemical Engineering, School of Chemical Engineering and Technology, Tianjin University, Tianjin 300072, China

Mingyan Liu
Dept. of Chemical Engineering, School of Chemical Engineering and Technology, Tianjin University Tianjin 300072, China
State Key Laboratory of Chemical Engineering, Tianjin 300072, China

Longfei Hui
Dept. of Chemical Engineering, School of Chemical Engineering and Technology, Tianjin University, Tianjin 300072, China

DOI 10.1002/aic.14015
Published online January 24, 2013 in Wiley Online Library (wileyonlinelibrary.com)

Micrometer–nanometer hydrophobic titania–fluoroalkylsilane composite coatings were prepared on substrates based on liquid-phase deposition. Coatings and crystallization forms were characterized with instruments of surface analyses. Experimental facilities of pool boiling were established to evaluate heat and mass transfer on coated surfaces in deionized water and saturated calcium carbonate solution. Obvious pool boiling enhancement was observed on thinner microscale–nanoscale hydrophobic titania–fluoroalkylsilane composite films at higher heat fluxes compared to that on thicker titania–fluoroalkylsilane coatings or on titania coatings and stainless steel surfaces. Lower fouling resistance was obtained on titania–fluoroalkylsilane coatings in pool boiling of saturated calcium carbonate solution and crystal form was aragonite, which was different from calcite on titania coatings. Results of inhibition of fouling and enhancement of heat transfer on titania–fluoroalkylsilane coatings were contributed to special surface microscale–nanoscale structure and material wettability. Asymptotic model was used to fit experimental data of fouling resistance, and reasonable agreement was obtained. © 2013 American Institute of Chemical Engineers *AIChE J*, 59: 2662–2678, 2013
Keywords: interfacial processes, evaporation, titania–fluoroalkylsilane, fouling, pool boiling

Introduction

The term "fouling" means any undesirable deposition on heat exchanger surfaces, which increases resistance to heat transmission.[1] The thermal conductivity of the crystallization fouling is often much less than that of the carbon steel, stainless steel (SS), or copper.[2,3] Hence, the accumulation of crystallization fouling can not only increase the power and energy consumption[4] and the initial investment and maintenance costs[5] but also affect the safe operation of the equipment and induce the corrosion of the heat-transfer surface.[6] As is shown by statistics, about 90% of the heat exchangers are facing the fouling problem to various degrees.[7]

The surface modification is one of the modern strategies to mitigate fouling by increasing the induction period and minimizing the fouling resistance.[8] Recently, surface coatings with different surface free energies have been tried to achieve antifouling targets, including Polytetrafluoroethylene (PTFE),[9] ion implantation (SiF_3^+, MoS_2, H^+, and F^-),[10] plasma chemical vapor deposition (SiO_x) or autocatalytic (Ni–P–PTFE[11,12] and Ni–Cu–P–PTFE[12]), reactive sputtering with TiN,[13] diamond-like carbon (DLC),[10,14] and TaC[10] coatings.

Generally, the poorest scale adherence should occur on materials with very low surface free energies.[15] Zhao et al.[12,16,17] studied $CaSO_4$ fouling properties of Ni–Cu–P–PTFE coating and F-DLC film and bacterial fouling features of Ni–Cu–P–PTFE coating and derived an optimum surface free energy using XDLVO theory. Zettler et al.[10] investigated the influence of the surfaces properties of the corrugated heat exchanger plates on the $CaSO_4$ fouling behavior and discovered that lower surface free energy generally led to less deposits formation, but surface free energy alone was not sufficient to describe the fouling behavior. Malayeri et al.[3] performed $CaSO_4$ scale experiments on spike-shaped hydrophobic nanostructured surfaces in micrometer thickness and demonstrated that these coatings significantly extended the induction time and decrease the fouling rate compared with the untreated AISI304 BA SS surface.

TiO_2 coating was applied to enhance boiling and to reduce fouling. Liu et al.[18] carried out several experiments of flow boiling of $CaCO_3$ solution on liquid-phase deposition (LPD) TiO_2 coatings in inner surfaces of seamless steel tubes and

Correspondence concerning this article should be addressed to M.Y. Liu at myliu@tju.edu.cn.

obtained that thinner TiO_2 coatings were more favorable for the heat transfer and inhibition of fouling. Wang and Liu[19] prepared TiO_2 coatings on copper substrates with inexpensive method of LPD and investigated $CaCO_3$ fouling characteristics in the pool boiling and corrosion behavior soaked in corrosive media on these coatings and preliminary antifouling and anticorrosion results were obtained and possible mechanisms was also explored.

Fluoroalkylsilane (FPS) was often used to prepare the hydrophobic and superhydrophobic coatings.[20] Hence, it is possible to prepare low-surface-free-energy coatings by FPS modification. However, Takata et al.[21] found that the film boiling could occur on superhydrophobic surface, which was detrimental to heat transfer. Hence, the coatings with moderate hydrophobicity or wettability would be favorable for fouling prevention as well as pool boiling enhancement.

As mentioned earlier, pool boiling as well as fouling investigations on TiO_2 coatings prepared by LPD on copper substrates were carried out, and encouraging results were obtained. However, no such a study is available on TiO_2–FPS composite coatings on SS substrates. The TiO_2–FPS composite coatings can obtain much lower surface free energy that is more favorable for the inhibition of fouling. What is more, the SS is a kind of widely used metal materials of heat exchangers. Hence, this article focuses on the characteristic researches of pool boiling and fouling simultaneously on microstructured and nanostructured hydrophobic TiO_2–FPS composite coatings deposited on polished substrates of AISI304 type SS with LPD method to develop novel surfaces of inhibition of fouling and enhancement of pool boiling. Meanwhile related mechanism will also be revealed. Coating thickness, roughness, contact angle, free energy, morphology, and chemical components and crystallization forms were characterized with various instruments for surface analyses. Advanced experimental installations of pool boiling with different coated surfaces were developed to evaluate the heat-transfer performances in deionized water and saturated $CaCO_3$ solution.

Experimental

This section mainly includes brief introduction on the coating preparation and characterization, pool boiling, and fouling experiments on various surfaces.

Preparation of TiO_2–FPS composite coatings

First, TiO_2 coatings with various film thicknesses were prepared with LPD technique on polished plate substrates.[22] The polished plate substrates were made of AISI304 type SS with diameter of 180 mm and thickness of 5.07 ± 0.02 mm. Then, TiO_2-coated plates were dipped into FPS-17 (Tianjin Yonglong Technology Development, Tianjin, China) hydrophobic solution to modify the TiO_2 coatings further to reduce the surface free energy before the plates were treated at high-temperature environment.

Characterization methods of coatings and crystal forms

Film thickness of transparent or translucent TiO_2 coatings was measured by the optical measuring instrument of thin film thickness (SGC-10, Tianjin Gangdong Scientific and Technical Development, Tianjin, China). Film thickness was obtained by fitting the interferometry spectrum formed by two reflection lights from coating surface and the interface between coating and substrate. When the shape of the measurement curve is similar to that of the fitting curve, the measurement result of the coating thickness is relatively accurate. The surfaces of both substrate and coating should have smaller roughness and only the thickness of the transparent or translucent TiO_2 coating could be measured with this measuring method.

Contact angles on coating surfaces were measured using the sessile drop method with video optical contact angle measuring instrument (OCA20, DataPhysics Instruments GmbH, Filderstadt, Germany) at 293 ± 1 K. Drop image was recorded using a high-speed CCD camera with a resolution of 768×576 pixels and up to 360 images per second. Standard liquids were water (doubly distilled), formamide (Tianjin Jiangtian Chemical, Tianjin, China) and diiodomethane ($\geq$98.0%, Tianjin Chemical Reagent Research Institute, Tianjin, China). Each injection volume of standard liquid was 2×10^{-9} m^3 (i.e., 2 μL). The droplet of the standard liquid was deposited on the surface and relaxed for 30 s. Then, the photo of the droplet was snapped. After that, the base line as well as the shape of the droplet was detected automatically by the contrast (bright-dark difference) of the drop to its surroundings, and then the contact angle of both sides of the droplet was automatically measured. At least 10 measurements were performed for each kind of the standard liquids.

There are two methods[23] for calculating the surface free energy: multiple liquids-two steps calculation method and system of equations method. The system of equations method can not only obtain nonpolar component γ^{LW} and polar component γ^{AB} but also γ_i^+ and γ_i^-.[24] Therefore, system of equations method was applied to calculate the surface free energy with one nonpolar standard liquid, diiodomethane, and two polar standard liquids, water and formamide.

Surface roughness was measured with JB-8C Roughness Tester (JB-8C, Guangzhou Guangjing Precision Instrument, Guangzhou, China). The vertical and horizontal displacement signal of the stylus can be obtained and converted to the form of a graph. The cut-off wavelength was set to 0.8×10^{-3} m, scan length 4.0×10^{-3} m, and scan speed 0.32×10^{-3} m s^{-1} during testing. To ensure the accuracy of the measurement results, at least five different locations on the same sample surface were selected randomly, and the average of the measurement results was calculated.

Surface morphology of the samples and fouling crystal forms were analyzed by the field emission scanning electron microscopy (FE-SEM, Nanosem 430, FEI). Pool boiling photos were obtained by a Complementary Metal Oxide Semiconductor (CMOS) high-speed camera system (BASLER A504k, 500–1000 fps, Germany). $CaCO_3$ foulant on the sample plate after fouling experiment was imaged with a Sony digital camera (SONY DSC-F717, Shanghai Suoguang Electronics, Shanghai, China).

Chemical elements in the coating were determined by the X-ray photoelectron spectroscopy (XPS) with a PHI 1600 ESCA (Perkin-Elmer) and energy dispersive X-ray spectroscopy (EDS). In the XPS analysis, an MgKα X-ray source was used. The instrument precision was ± 0.15 eV, and the pressure in the chambers during the experiments was about 2.66×10^{-8} Pa. The X-ray photoelectron spectra were referenced to the C1s peak ($E_b = 284.60$ eV). The specimens were sputtered with Ar^+ for 30 s to clean the surfaces. The spectral data were quantitative analyzed by the self supplied simulation software.

Preparation of calcium carbonate solution

Solid $CaCO_3$ is an insoluble salt in water. $CaCO_3$ solution was prepared by mixing a certain quantity of calcium chloride

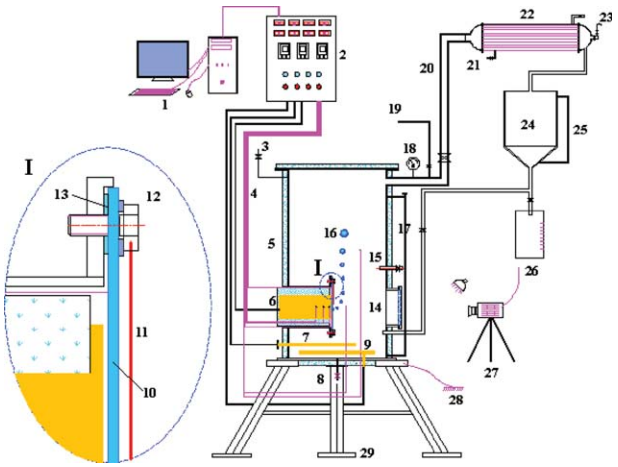

Figure 1. Schematic diagram of pool boiling apparatus.

(1) Online acquisition and control system; (2) control cabinet and power supply; (3) solution inlet; (4) thermocouple of T1–T5; (5) heat insulation layer; (6) copper heating unit; (7) straight tube heater; (8) solution outlet; (9) spiral tube heater; (10) coated plate; (11) reference line for bubble size measurement; (12) bolt; (13) heat-resistant silicone gasket; (14) sight glass; (15) solution sample outlet; (16) vapor bubble; (17) liquidometer; (18) pressure gauge; (19) vapor vent; (20) vapor pipe with heat insulation; (21) cooling water system; (22) vapor condenser; (23) relief valve; (24) condensate storage tank; (25) liquidometer; (26) metering tank; (27) CMOS measuring system; (28) ground connection; and (29) boiling pool holder. [Color figure can be viewed in the online issue, which is available at wileyonlinelibrary.com.]

($CaCl_2$) and sodium bicarbonate ($NaHCO_3$) in deionized water[25] with temperature of 293±1 K. The molar ratio of the former to the latter is 0.5. All chemicals used are of analytical grade. The solution concentration was measured with the ethylene-diamine-tetra-acetic-acid titration method using calcium-carboxylic as acid indicator.[26] The pH value of the solution was measured by the portable pH meter (PHB-4, Shanghai Precision Scientific Instrument, Shanghai, China).

Experiments, measurements, and uncertainty analyses

The schematic diagram of the pool boiling apparatus is shown in Figure 1. All the equipment parts and pipelines contacted with test liquids were made of AISI304 SS. The apparatus consists of a test plate with diameter of 0.18 m, a cylindrical pool, a closed loop system containing a condensing section, a cylindrical copper heater with a power control unit, a solution injection unit, an auxiliary heating system, an online data acquisition system, and a 500 fps CMOS camera system. Boiling phenomena on the plate surface was observed through a front sight glass or two side sight glasses in the cylindrical pool. The cylindrical copper heater was mounted horizontally with one end contacting with the plate. A safety relief valve was fitted at the top of a shell-and-tube condenser with tap water as cooling media to release the pressure in the event of a pressure excursion due to failure in cooling or out of work of the silicon controlled rectifier. A straight tube and a spiral auxiliary heater located at the bottom of the pool to preheat the bulk liquid and to compensate the heat loss of the apparatus. The vapor condensate returned to the bottom of the pool and was heated by the auxiliary heater. The boiling pool, copper heater, and vapor pipe were insulated to reduce heat loss to the ambient air. All the temperatures including the bulk temperature of $CaCO_3$ solution were measured with high-accuracy thermocouples. The heat flux through the plate surface was controlled by changing the electric voltage of the copper heater. Three E-type thermocouples were fitted equidistantly along the axial central line of the copper rod. One of the thermocouple connected to the temperature controller to cut off the heating power unit if the internal temperature of the heater exceeded the temperature limitation. This feedback control ensured heat flux stable. Three pairs of parallel holes were drilled in the plate to measure the surface temperature of the test plate, as shown in Figure 2. A visual software interface was edited with the Visual Basic computer language for online data acquisition system, which realized real-time monitoring of the test results on the computer screen. $CaCO_3$ solution with given concentration was injected in the pool for each fouling test. Pool boiling and fouling experiments were carried out in the nucleate boiling regime at atmospheric pressure. At least three times of fouling solution samples were taken every 1800 s during the pool boiling fouling tests to measure the $CaCO_3$ concentrations. The plate was cut into small samples at the end of the tests to analyze the fouling morphology and chemical composition. $CaCO_3$ foulant on sample plate was taken with a digital camera.

It is noted that the pressure of the boiling pool could not maintain atmospheric pressure during the fouling tests (especially at the initial time) if all of the outlets of the pool boiling system were closed, because of the continuous escape of CO_2 gas from the fouling solution. Hence, the condensate outlet valve was open during the tests to ensure the pool boiling system under atmospheric pressure condition. The vapor condensate discharged constantly and the level of the fouling solution declined slowly as the fouling test went on. The fouling experiment finished when the solution level was slightly lower than the highest point of the vertical coating plate. In other words, the coating plate was still completely immersed in the fouling solution.

Heat flux through the hot plate was obtained with a two-dimensional heat conduction theory, because the diameter of the plate is larger than that of the heating copper rod. The plate was divided into two regions, the circular surface with the diameter of 0.103 m in the central, and the remaining ring area between the diameters of 0.103 and 0.180 m, as shown in Figure 2a. The distribution of the heat flux along the radial and axial directions within the plate was numerically calculated with ANSYS V14.0 software (ANSYS).

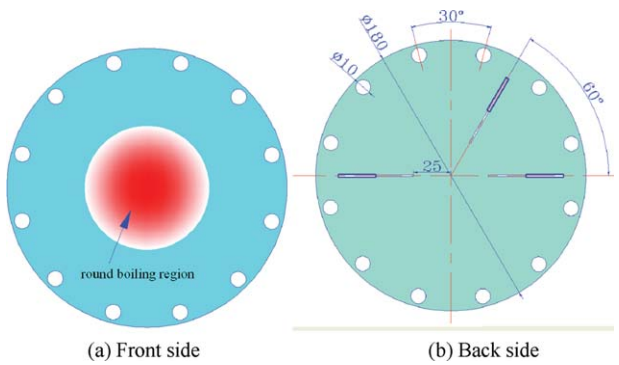

(a) Front side (b) Back side

Figure 2. Front and back sides of the hot plate (unit: 10^{-3} m).

(a) Front side and (b) back side. [Color figure can be viewed in the online issue, which is available at wileyonlinelibrary.com.]

Table 1. The Main Experimental Variables

Heat-Transfer Diameter and Thickness of Test Plate (m)	Diameter and Length of Copper Heater (m)	Diameter and Length of Boiling Pool (m)	Tube Number, Diameter and Length of Condenser (m)	Concentration Range of $CaCO_3$ Solution (10^{-3} kg m^{-3})	Heat Flux Range (kW m^{-2})
0.103 × 0.005	0.07 × 0.2	0.26 × 0.55	19 × 0.016 × 0.32	65–750	2.71–70.05

Simulation results of the heat flux distributions indicated that about 90.2% heat flowed in the axial direction of the plate. Therefore, the heat flux was calculated with the product of electric current I, voltage U, and divided by the circular surface area, and then multiplied by the factor of 0.902.

The main experimental variables are listed in Table 1. The fouling resistance, R_f, was calculated from the heat-transfer coefficients at the beginning of each experiment and the actual heat-transfer coefficients after a certain running time according to the following equation[27]

$$R_f = \frac{1}{\alpha_t} - \frac{1}{\alpha_0} \quad (1)$$

where α_t is the overall heat-transfer coefficient for the fouling and α_0 for the clean surface.

The heat-transfer coefficient is defined as[27]

$$\alpha = \frac{\dot{q}}{T_w - T_b} \quad (2)$$

Electrical voltage was measured with a 2.5 grade voltmeter with instrument precision of ±0.5 V, and the current was measured with a 2.5 grade ampere meter with accuracy of ±0.05 A. The diameter of the copper cylindrical was measured with a vernier caliper with the accuracy of ±0.02 × 10^{-3} m. The maximum uncertainty for measuring the heat flux is 5.15%. The heat flux was validated with the volume of steam condensate per unit time. Compared with the calculated value, the maximum error is 6.99%, and the minimum error is 2.69% in the entire range of the heat flux. The vapor pressure was measured with a pressure gauge. The factory calibrated uncertainty was estimated to be 1.5% of the operating range with 95% confidence for the pressure gauge, the ammeter, and the voltmeter. All the five thermocouples were calibrated with second standard precision mercury thermometer with the accuracy of ±0.01 K to eliminate the systematic error. After calibration, the thermocouples did not exceed the measurement error of ±0.2 K. Minimum and maximum errors for the evaluated heat-transfer coefficients are 5.43 and 6.69%, respectively. Average heat loss of the apparatus in the course of the experiments is 6.42%. The auxiliary heater was kept open with the minimum heat flux during the experiments to maintain the bulk solution at a saturation point and to compensate the heat loss of the apparatus into the ambient air.

Details of the experimental design and parameter measurement are shown in Appendix.

Results and Discussion

Coating characterization

Three sample plates of TiO_2 coatings (B, C, and D) with different thicknesses were prepared. The sample plates of B, C, and D were further treated with FPS-17 hydrophobic solution, which were named after BF, CF, and DF, respectively. The polished SS was chosen as a control sample for comparison analyses. The sample plates were characterized.

Coating thickness

The thicknesses of TiO_2 coatings on the samples of B, C, and D were 104.7±0.5 × 10^{-9} m, 159.1±2.5 × 10^{-9} m, and 204.9±2.8 × 10^{-9} m, respectively. The thickness of FPS layer formed on TiO_2 coatings was less than 2 × 10^{-9} m.[28] Therefore, the thickness of TiO_2–FPS composite coatings equaled to that of TiO_2 coatings.

Surface morphology and chemical elements of coatings

FE-SEM. Figure 3 shows FE-SEM images of polished SS, TiO_2, and TiO_2–FPS composite coatings. TiO_2 coatings B and C consist of porous grains with a few tens of nanometers. TiO_2 coating C is denser than coating B. The nanoscale holes might be available for the nucleation sites of bubbles in the pool boiling. TiO_2 coating D consists of many large particles and almost no pores are found on the surface. The large particles might provide crystal nuclei for the fouling deposition. TiO_2–FPS coating CF became denser after modification compared with TiO_2 coating C.

EDS. EDS analyses were carried out on TiO_2–FPS composite coating CF, as shown in Figure 4. Elements of Ti, F, and Si were detected on the coating, and corresponding values of atom percentage (at. %) are 2.81, 5.42, and 1.52%, sequentially. Fe, Cr, Mn, and Ni elements from SS substrate were also observed, because the depth of electron beam irradiation is several microns that are far greater than the thickness of sample CF. Trace Al element in the coating surfaces might come from the polishing paste, because the polished SS substrate used for coating preparation might not be completely cleaned. The raw material of Al came from the corundum that is the main components of the polishing paste.

XPS. Typical spectrum of TiO_2 coating B surface is presented in Figure 5. Ti2p3, Ti2p1, Fe2p, Cr2p, and O1s photoelectron peaks were observed. C1s peak at the binding energy of E_b=284.5 eV is of carbon from a thin contamination layer.[29] The percentage values of Ti and O elements in coating B are 25.2 and 56.1%, respectively. The ratio of O to Ti is 2.23, which is slightly higher than the atomic stoichiometry of TiO_2. The result means that parts of the O atoms have combined with other elements, such as Fe and C. It is obviously shown in Figure 5 that the background of the photoemission peaks at high binding energy is higher than that at low one. The peaks of CKLL, TiLMM, and OKLL belong to the auger electron spectroscopy (AES), which is often the concomitants of the XPS peak. The analysis of AES peaks is not included.

Ti2p region can be decomposed into several contributions corresponding to the different oxidation states of titanium as shown in Figure 5b, because the values of binding energy of Ti2p3 and Ti2p1 peaks are very close. Each contribution consists of a doublet of 2p3/2 and 2p1/2 peaks. The main doublet composed of two symmetric peaks situate at E_b (Ti2p3/2)=458.7 eV and E_b (Ti2p1/2)=464.4 eV,

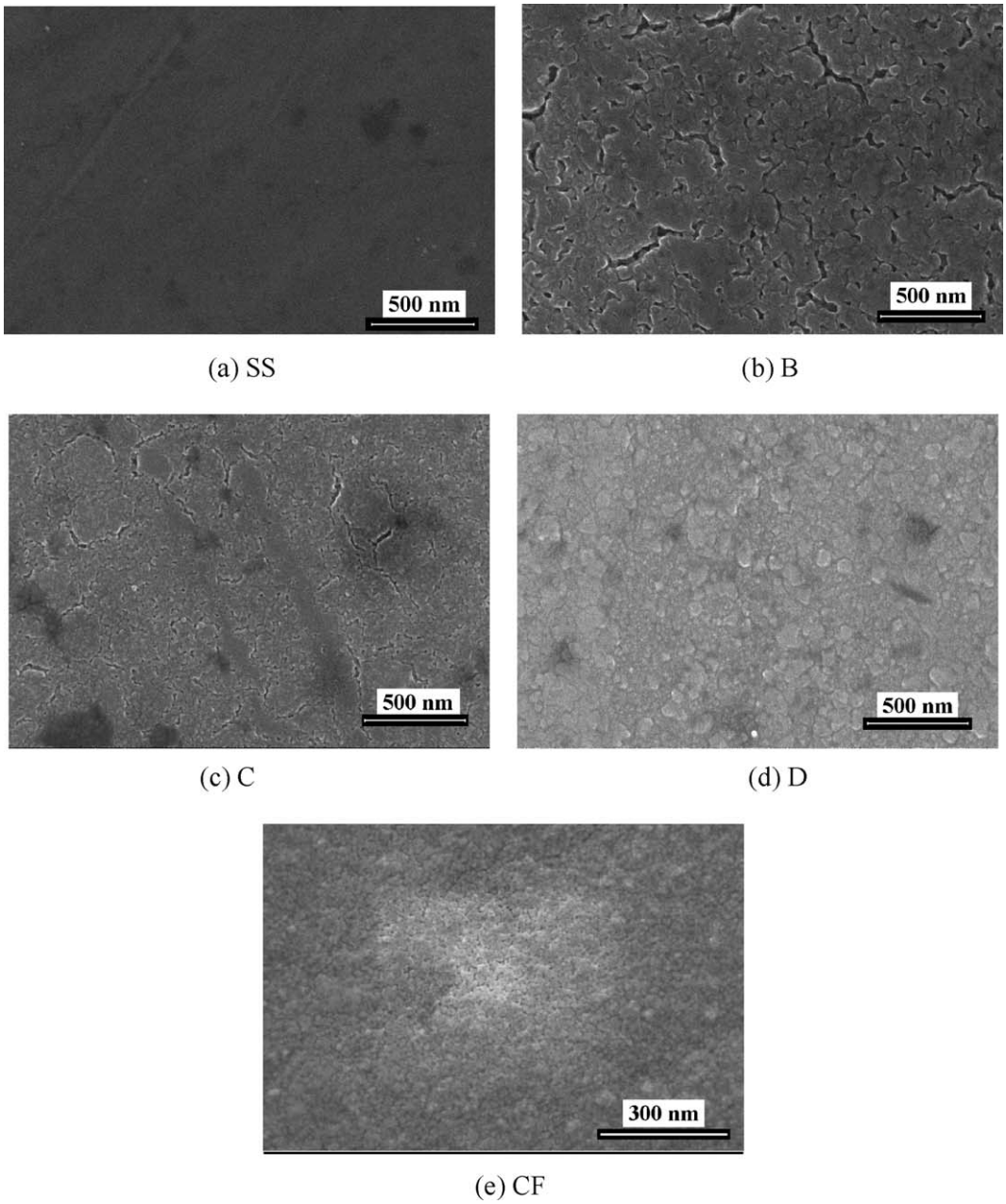

Figure 3. FE-SEM images of polished SS, TiO_2, and TiO_2–FPS coating surfaces (1 nm=10^{-9} m).

(a) Polished SS; (b) TiO_2 coating B (thickness 104.7 × 10^{-9} m); (c) TiO_2 coating C (159.1 × 10^{-9} m); (d) TiO_2 coating D (204.9 × 10^{-9} m); and (e) TiO_2–FPS coating CF (159.1 × 10^{-9} m). [Color figure can be viewed in the online issue, which is available at wileyonlinelibrary.com.]

respectively, which are the typical XPS spectra of Ti(IV). The area ratio of these two peaks, $A_{(Ti2p1/2)}/A_{(Ti2p3/2)}$, is approximately equal to 0.5, and the binding energy difference, $\Delta E_b = E_b(Ti2p1/2) - E_b(Ti2p3/2)$, is about 5.7 eV, which is the same as previously reported value (Pouilleau et al., 1997). The simulation results in Figure 5c show that titanium element in the coating possesses not only Ti (IV) but also Ti (II) and Ti (III). The peak area ratio of Ti (II):Ti (III):Ti (IV) is 1:1.42:2. That is, the content of Ti (IV) in the coating accounts for about 45.2% of the total number of Ti atoms. The results show that 43.3% of the Ti (IV) atoms in the TiO_2 coating reduce to the lower valences.

The reduction of Ti element could be attributed to two main reasons. The first one may be the presence of residual carbon on the coating layer. The carbon burnt and drew oxygen from the surrounding atmosphere and the layer network during the heat treatment, which made Ti (IV) reduce to Ti(III), and a small amount of Ti(IV) and Ti(III) reduce to Ti(II). The second may be Ti(IV) and Ti(III) that are easily reduced to Ti(II), as the TiO_2 surface was bombarded with argon ions.[30]

The XPS spectrum of coating BF is shown in Figure 6. It can be seen from Figure 6 that, the binding energy of 102.6 eV for Si2p orbit electrons was excited, which is the characteristic peak of the Si—O bond. Moreover, the XPS peaks at the binding energies of 529.4 and 532.5 eV correspond to the O element in the O—Ti and O—Si bonds, respectively, and the peaks at the binding energies of 458.7 and 464.9 eV correspond to the Ti element in the T—O bonds. The binding energy of 688.9 eV belongs to —CF2 bond groups. In other

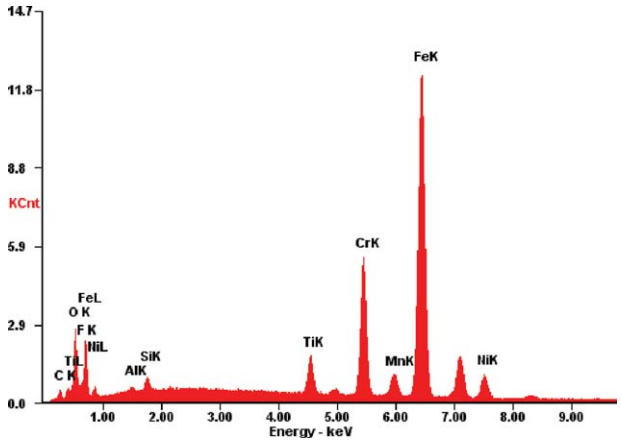

Figure 4. EDS of TiO_2–FPS coating CF with film thickness of 159.1 × 10^{-9} m.

[Color figure can be viewed in the online issue, which is available at wileyonlinelibrary.com.]

words, the Ti—O bond came from the TiO_2 coating, and the Si—O bond was the chemical bond connected between the FPS and the TiO_2 coating, whereas the —CF2 group came from the FPS coating.

Contact angle and surface free energy

Calculated surface tension components (γ_s^{LW}, γ_s^+, and γ_s^-) as well as the polar energy component (γ_s^{AB}) and the total free energy component of each surface (γ_s) are shown in Table 2.

It can be seen from Table 2 that the contact angles increase greatly, and the surface free energies of TiO_2–FPS composite coatings reduce sharply. This result is consistent with many other researchers' findings. Takata et al.[31–33] prepared TiO_2 and TiO_2–SiO_2 coatings on copper/glass substrates, obtained superhydrophilic surface. Wasserman[34,35] prepared silane monolayer on Si/SiO_2 substrate using chlorosilane hydrolysis and greatly improved hydrophobicity of substrate. Zhang et al.[36] modified various material surfaces

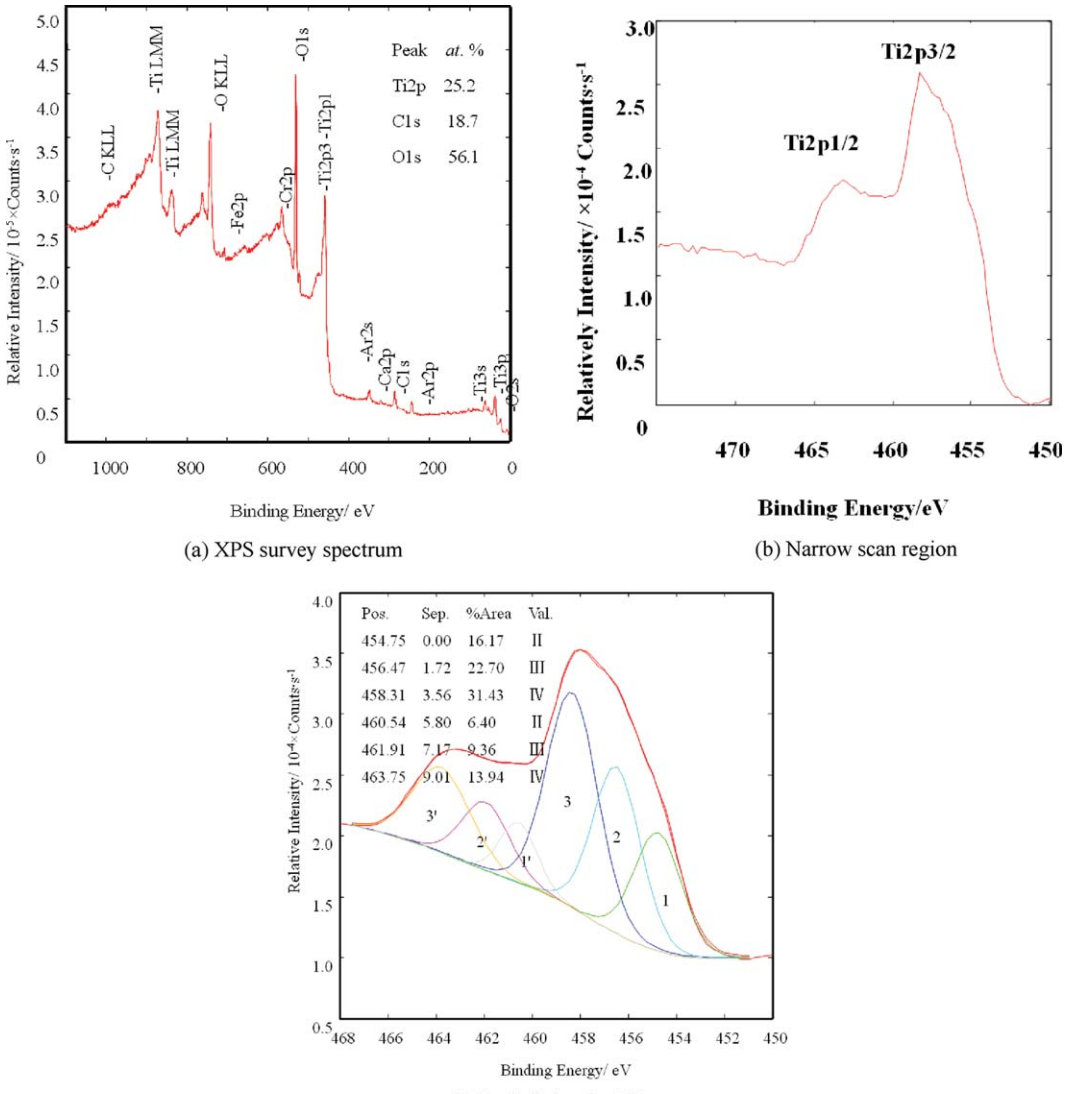

Figure 5. XPS spectra of TiO_2 coating B with film thickness of 104.7 nm and fitting results for Ti2p region.

(a) XPS survey spectrum; (b) narrow scan region; and (c) peak fitting for Ti2p. [Color figure can be viewed in the online issue, which is available at wileyonlinelibrary.com.]

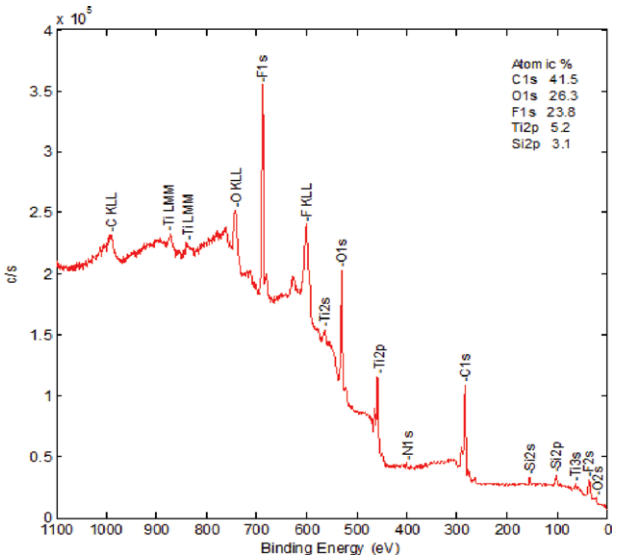

Figure 6. XPS spectrum of TiO_2–FPS coating BF with film thickness of 104.7×10^{-9} m.

[Color figure can be viewed in the online issue, which is available at wileyonlinelibrary.com.]

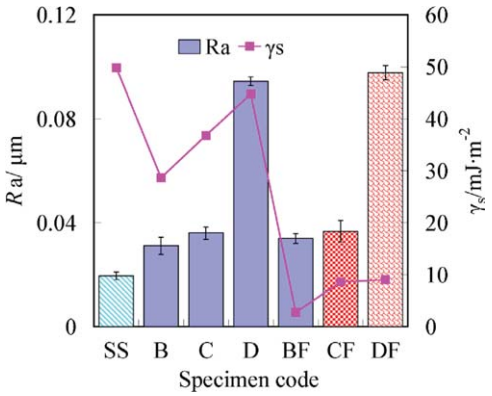

Figure 7. Surface roughness and free energy of various sample surfaces (1 μm=10^{-6} m; 1 mJ=10^{-3} J).

SS: AISI304 SS; B–D: TiO_2 coatings with the values of film thickness of 104.7, 159.1, and 204.9 × 10^{-9} m, respectively; BF, CF, and DF: TiO_2–FPS composite coatings corresponding to TiO_2 coatings of B, C, and D, respectively. [Color figure can be viewed in the online issue, which is available at wileyonlinelibrary.com.]

with tridecafluoro-octyl triethoxysilane/heptadecafluoro Kwai triethoxysilane, of which the contact angle increased to about 110°. It is known that the crystal structure of the surface, the presence of small quantities of impurities in the metal, the roughness of the surface, and the presence of oxide on the surface may alter the effective surface free energy.[15] In addition, the surface free energy, obtained from contact angle measurements, also depends on the calculation method.[23]

Surface texture profile

The results of the surface roughness of different samples are shown in Figure 7. To find the relation between the surface roughness and the surface free energy of the coatings, the calculation results of total free energy component are also shown in Figure 7. The surface roughness of polished SS surface is very low, but the surface free energy is relatively high. Surface roughness and free energy increases with the increase of the coating thickness with regard to the coatings of B, C, and D. However, the reason for the correlation between the surface properties and the coating thickness is not clear. The surface free energy of the TiO_2 coating decreases sharply when treated with the FPS hydrophobic solution. But the surface roughness does not change too much. The reason is that the FPS hydrophobic film is of a self-assembled monolayer,[28] which has little effect on the surface morphology.

Pool boiling investigations of deionized Water

Figure 8 shows the variation of the heat-transfer coefficient with the heat flux for pool boiling of deionized water on the coatings of C and D as well as microscale–nanoscale hydrophobic composite coatings of CF and DF. Figure 9 shows the percentage change of the heat-transfer coefficient on the coatings compared with SS substrate at different heat fluxes. The results show that thinner TiO_2 coating C enhance pool boiling obviously, especially at higher heat flux, because there are more nanoscale cavities and cracks on these three surfaces (see Figure 3), which could provide more nucleation sites for bubble formation in the pool boiling than polished SS surfaces; thicker coating D on the other hand deteriorates the heat transfer might due to the low thermal conductivity of TiO_2 material and dense coating.[37] These findings are consistent with those reported in the literature.[19]

Figures 8 and 9 also indicate that pool boiling on hydrophobic TiO_2–FPS coatings CF was improved compared to that on TiO_2-coated surface F, although the values of the surface roughness of C and CF are the same. There are generally three mechanisms contributing to the nucleate pool boiling: vapor bubble generation and departure from nucleation sites on the superheated surface, microlayer evaporation underneath the bubbles, and natural convection on inactive nucleation areas of heated surface and the heat transfer due to the first two mechanisms accounts for about 90% of the total heat flux.[38] The boiling coefficient has a positive

Table 2. Contact Angle and Surface Free Energy of Different Surfaces

	Contact Angle (°)			Surface Free Energy (10^{-3} J m^{-2})				
Specimen	θ_w	θ_f	θ_d	γ_s	γ_s^{LW}	γ_s^{AB}	γ^+	γ^-
SS	46.7±4.0	29.8±4.2	48.3±3.1	49.83	28.33	21.50	4.38	26.40
B	93.2±10.1	65.8±8.3	78.4±5.3	28.66	26.64	2.02	1.36	0.75
C	84.5±9.8	52.8±6.6	48.3±5.3	36.78	33.67	3.21	1.85	1.39
D	63.7±7.9	42.1±4.3	55.0±4.5	41.37	26.84	14.53	4.10	12.86
BF	137.2±4.7	128.4±2.4	121.4±6.3	2.76	2.76	0	0	0.14
CF	124.8±4.0	122.9±7.8	104.2±1.4	8.58	6.29	2.29	0.56	2.33
DF	117.1±2.6	111.3±2.2	98.4±7.9	9.02	8.17	0.86	0.08	2.43

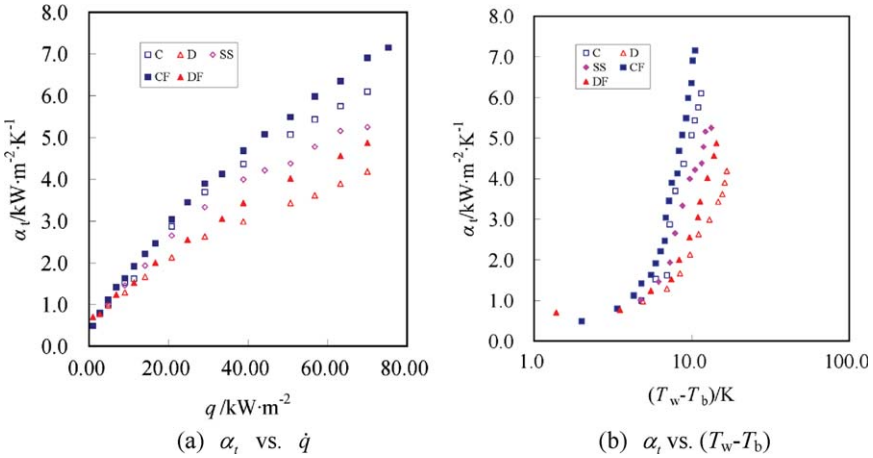

Figure 8. Pool boiling coefficients of deionized water on various surfaces.

SS: AISI304 SS; C and D: TiO_2 coating with thickness of 159.1 and 204.9 × 10^{-9} m, respectively; CF and DF: TiO_2–FPS composite coatings. (a) α_t vs. $\dot{q}$ and (b) $\alpha_t$vs. (T_w-T_b). [Color figure can be viewed in the online issue, which is available at wileyonlinelibrary.com.]

relationship with the active nucleation site density.[39] The work required for vapor bubbles creation on hydrophobic surface is very small. Thus, the vapor bubbles are more likely generated on the hydrophobic surface.[40] Therefore, more bubbling sites were observed, and higher pool boiling coefficient was available on TiO_2–FPS composite coatings.

However, heat-transfer coefficient on hydrophobic coating of DF is lower than that on polished SS surface at the same heat flux, although the surface free energy of coating DF is very low. On the one hand, low surface free energy promotes the number of the bubbles formed on the surface. However, dense and thick coating with a low thermal conductivity might provide additional thermal resistance. The factors of surface free energy, roughness, materials, and morphology should be considered comprehensively for explaining the pool boiling phenomena.

Typical boiling photographs obtained with CMOS camera on the surfaces of SS, C, CF, and D at the heat flux of 50,690 W m^{-2} are shown in Figure 10. C, D, and CF were chosen to represent TiO_2 and TiO_2–FPS coatings, respectively, because the same kind of coatings possesses similar performance. Average departure bubble diameter on the surface was statistically calculated with Image-Pro Plus software (version 6.0, Media Cybernetics). Vapor bubble waiting and growth periods were estimated according to the image sequences of vapor bubbles. No less than five vapor bubble sites on heat-transfer surface and no fewer than three sequences for each bubble were chosen to calculate the vapor bubble parameters. Estimated vapor bubble dynamic parameters on various surfaces are shown in Table 3.

It can be found in Figure 10 that the density of nucleation sites on CF surface is far greater than that on other surfaces during pool boiling. The diameters of vapor bubbles are small, and the nucleation sites distribute uniformly on CF surface, as shown in Table 3. The departure frequency of vapor bubble on CF surface is 83.3 Hz, which is the highest value. Large nucleation site density, small-size bubbles, and high bubble departure frequency on CF surface are all in favor of pool boiling enhancement. In addition, average growth time, $\bar{t}_g$, is double of the waiting time, $\bar{t}_w$, on CF surface. These results of vapor bubble dynamics on CF are similar to those on the low energy surface of Teflon.[41] There are fewer formation sites and larger departure diameter of vapor bubbles on D surface (see Figure 10d) and average departure diameter of vapor bubbles is 4 × 10^{-3} m with the detachment frequency of about 12.3 Hz, which is lower than that on the other surfaces. The average waiting time of vapor bubbles is about 1.5 times as long as the growth time during the bubbles formation and growth on D surface, which means that the natural convection takes more than half of the total time of heat transfer process on the single bubble formation site. Such a low detachment frequency and long waiting time of vapor bubbles is detrimental to the pool boiling.

The average departure diameter of vapor bubbles on C surface is about 1.8 × 10^{-3} m, and the departure frequency of vapor bubbles is about 35 Hz, which is larger than that on polished SS surface. It is surprising that the growth time of

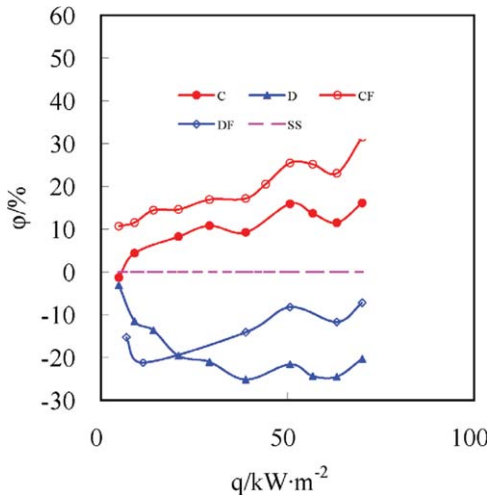

Figure 9. Percentage change of heat-transfer coefficient on various coated surfaces compared to polished SS at different heat fluxes (SS: AISI304 SS; C and D: TiO_2 coating with thickness of 159.1 and 204.9 × 10^{-9}m, respectively; CF and DF: TiO_2–FPS composite coatings).

[Color figure can be viewed in the online issue, which is available at wileyonlinelibrary.com.]

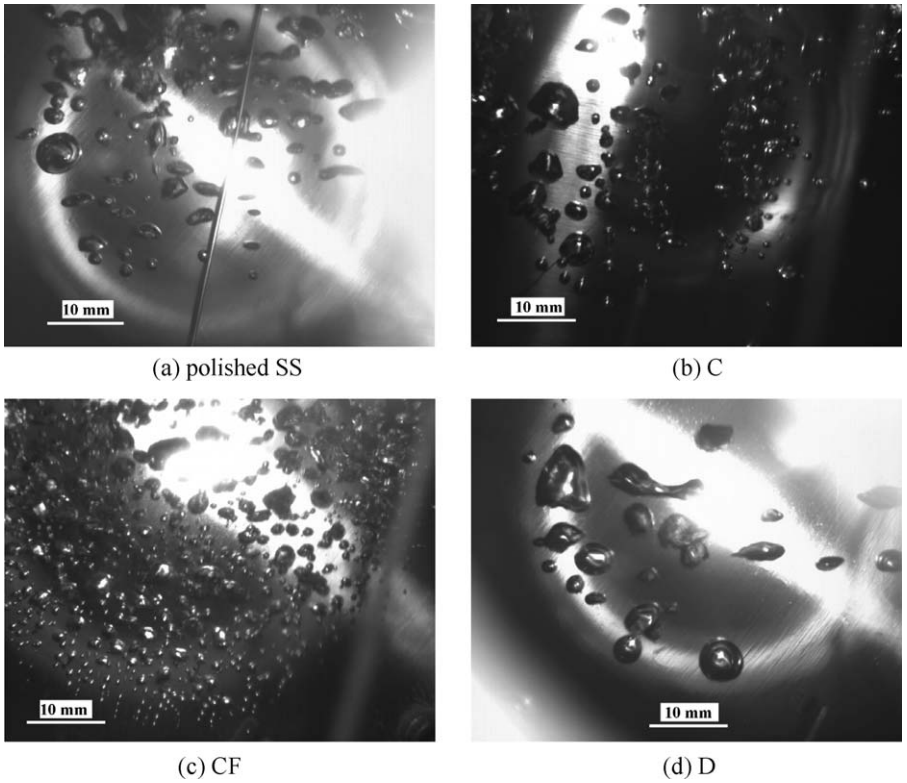

(a) polished SS (b) C

(c) CF (d) D

Figure 10. Photographs of boiling vapor bubbles on different plates at heat flux of 50,690 W m^{-2}.

(a) Polished SS; (b) C; (c) CF; and (d) D.

the bubbles is equal to the waiting time on coating C. However, the waiting time of the bubbles on SS surface is about three times as long as the growth time. The formation and growth of the vapor bubbles were always at the fixed nucleate sites throughout the pool boiling. The bubbles on the surface with larger departure diameter might have a longer waiting time and lower departure frequency, as shown in Table 3.

In addition, the bubble shape on coating CF is hemispherical, whereas the shape on coating D is oblate, as shown in Figures 10c,d. According to the literature,[42] the shapes of departure bubbles are controlled by the surface tension force and the inertial force. When the surface tension force dominates the departure, the bubble tends to be spherical. However, when the inertial force dominates, the bubble tends to be hemispherical, and when both forces are significant the bubble has an oblate shape.

Pool Boiling Fouling

Fouling on different coating surfaces. Figure 11 shows fouling resistance vs. time on various surfaces in pool boiling of $CaCO_3$ solution. Corresponding asymptotic fouling resistance values are shown in Figure 12.

From Figure 11, one can find that the relationships between fouling resistances and time on all surfaces exhibit asymptotic trends. For the same coating material, asymptotic fouling resistance increases with the increase of surface free energy and roughness. All the asymptotic fouling resistances of coated surfaces are less than that of the polished SS substrate, except for coating D surface. Large surface roughness and TiO_2 particles are observed on the D surface as shown in Figure 4d, which might serve as many crystal nucleuses for $CaCO_3$ crystallization. Meanwhile, high surface free energy of D also contributes to the high asymptotic fouling resistance. Polished SS surface has a high asymptotic fouling resistance due to its high surface free energy, although its surface roughness is very low. The asymptotic fouling resistance of coating DF is less than that of D due to its lower surface free energy and roughness. Lower surface roughness provides fewer nucleation sites for $CaCO_3$ crystallization, whereas lower surface free energy results in lower surface temperature and less fouling deposition.[10]

Negative fouling resistances were observed at the early stage of the fouling curves due to a small amount of foulant deposition on the surface, as shown in Figure 11. The initial fouling deposition on the surface provides nucleation sites for bubble formation and increases the turbulence level near the surface.[27] Therefore, initial boiling coefficients are slightly higher than those coefficients of clean surface at the initial stage of the fouling test.

Table 3. Parameters of Vapor Bubble Dynamics on Different Heat-Transfer Surfaces

Sample	$\bar{D}_d$ (10^{-3} m)	$\bar{f}$ (Hz)	$\bar{t}_g$ (10^{-3} s)	$\bar{t}_w$ (10^{-3} s)	$\bar{t}_g+\bar{t}_w$ (10^{-3} s)
SS	2.7±0.5	24.8±0.9	9.6±0.9	30.8±1.0	40.4±0.9
C	1.8±0.3	34.5±0.6	14.5±0.5	14.5±0.8	29.0±0.6
CF	0.8±0.1	83.3±0.2	8.0±0.1	4.0±0.2	12.0±0.2
D	4.0±0.8	12.3±1.1	32.2±1.1	48.9±1.0	81.1±1.0

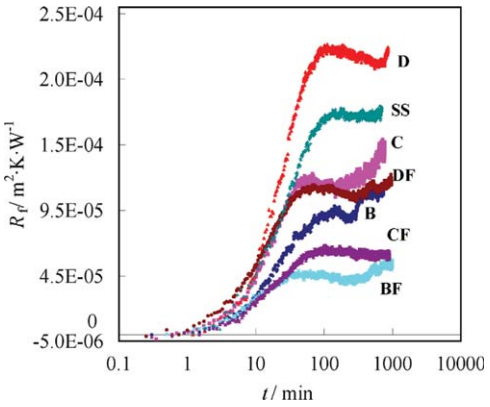

Figure 11. Fouling curves on various surfaces at heat flux of 50,690 W m^{-2} and initial $CaCO_3$ concentration of 0.25 kg m^{-3} (i.e., 250.0 mg L^{-1}) (1 min=60 s).

[Color figure can be viewed in the online issue, which is available at wileyonlinelibrary.com.]

Spots of $CaCO_3$ fouling on various plates after fouling experiments are shown in Figure 13. These points are the sites where the vapor bubbles appeared, and the crystals deposited on the surfaces in the pool boiling. $CaCO_3$ is an inversely soluble salt, and the temperature under the vapor bubbles is higher than that at other positions of the plate surface. Deposits with fairly high density and large adherence tendency are easily deposited under the vapor bubbles. Hence, a hard and whitish-colored deposit formed on the regions where the nucleation boiling occurred (region I in Figure 13a) and a smooth, semitransparent fouling layer formed in the relatively undisturbed region between the nucleation boiling sites (region II). The loose fouling around each nucleation boiling site was found on the C surface, as shown in Figure 13b. Many small and fluffy fouling points were found on the CF surface as shown in Figure 13c. A mass of vapor bubbles with small departure diameters were formed on the composite surface during pool boiling. The interaction between the fouling particles and the composite surface was poor due to its very low surface free energy, and the fouling was easily removed from the surface. Large fouling points were found on the thick TiO_2 coating, as shown in Figure 13d. These fouling points attributed to the big vapor bubbles formed on the surface during the pool boiling. The pool boiling on the plate was inhibited probably by the thick TiO_2 coating according to Liu's finding.[18] A higher surface temperature reached, and denser, harder, and more adherent fouling points were formed on the surface.

FE-SEM morphology and EDS element analyses of $CaCO_3$ crystals on the coatings of C and CF are shown in Figures 14 and 15.

Calcium carbonate has three polymorphs: calcite (trigonal crystal system), aragonite (orthorhombic), and vaterite (hexagonal). Five or six prismatic crystals of $CaCO_3$ deposited on coating C surface, as shown in Figure 14b. The fouling is very incompact, much fragile, and easy to remove. The crystal form of the fouling on coating C is calcite.[43] The lanceolate structure of the fouling was found on the CF surface, as shown in Figure 15. The crystal form of the fouling on coating CF is aragonite[43] and easy to clean away. The amounts of the fouling crystals on the unit area of the CF surface are much less than that on the coating C. Meanwhile, the crystal size on the coating CF surface is much larger than that on the coating C, as shown in Figures 14b and 15b. The reasons for different crystal forms on the C and CF surfaces might be expressed as the following. There were more vapor bubbles in small size and, thus, more nucleation sites on the CF surface than on the C surface. The temperature under the vapor bubbles was higher than that at the other positions on the surface. The solution supersaturation degree under the vapor bubbles was greater than that at the other positions. It was reported that aragonite crystal was easy to precipitate at higher supersaturation degree than calcite crystal.[44–46] Therefore, the aragonite crystals were found on the CF surface and calcite crystals on the C surface. The results also indicate that surface modification is a method to change the polymorphs of $CaCO_3$.

Fouling in different concentrations of $CaCO_3$ solution

Relationship between fouling resistance and time on coating C with various initial $CaCO_3$ concentrations at heat flux of 50,690 W m^{-2} are shown in Figure 16, and the variation of $CaCO_3$ concentration in bulk solution with time is also included in Figure 16. It can be seen from Figure 16a that the fouling resistance for each concentration increased obviously at the initial time of the test and then reached an asymptotic value. Initial $CaCO_3$ concentration affected fouling resistance significantly, and a higher $CaCO_3$ concentration leaded to a higher asymptotic fouling resistance. It can be seen from Figure 16b that although $CaCO_3$ concentration in bulk solution at initial time was very high, the concentration decreased significantly with time and after about 7200 s (i.e., 120 min), all the initial concentrations reduced to and kept about 0.03 kg m^{-3}. The phenomenon results from properties of $CaCO_3$. As insoluble salts, $CaCO_3$ solution was prepared by $CaCl_2$ and $NaHCO_3$ to obtain fouling solution of high concentration. During the process in which the solution was heated to saturation temperature, $CaCl_2$ reacted with $NaHCO_3$ rapidly and formed $CaCO_3$ solid particles and, thus, decreased the $CaCO_3$ concentration in fouling solution. With the decrease of $CaCO_3$ concentration, the rate of decrease slowed down gradually. However, the sharply decreases of $CaCO_3$ concentration showed significant influence on the degree of $CaCO_3$ super saturation. A lot of

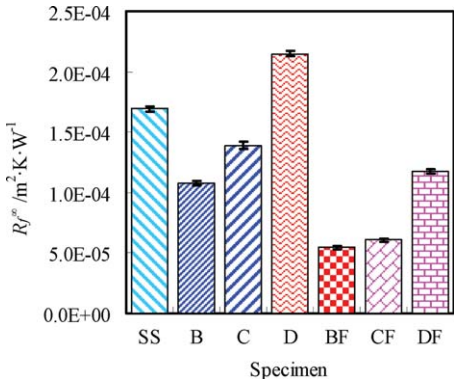

Figure 12. Asymptotic fouling resistances on different specimen surfaces (SS: AISI304 SS; B–D: TiO_2 coating with thickness of 104.7, 159.1, and 204.9 × 10^{-9}m, respectively; BF, CF, and DF: TiO_2–FPS composite coatings).

[Color figure can be viewed in the online issue, which is available at wileyonlinelibrary.com.]

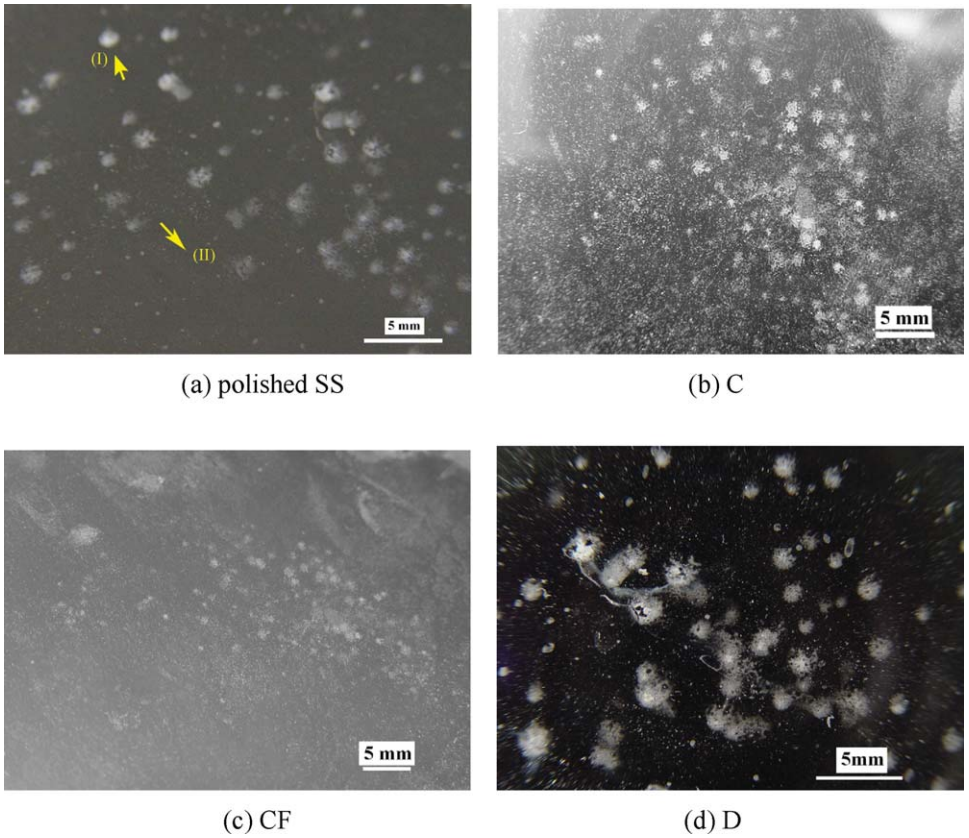

(a) polished SS (b) C

(c) CF (d) D

Figure 13. Experiment observations of $CaCO_3$ fouling points on various plate surfaces (1 mm=10^{-3} m).

(a) polished SS; (b)C; (c) CF; and (d) D. [Color figure can be viewed in the online issue, which is available at wileyonlinelibrary.com.]

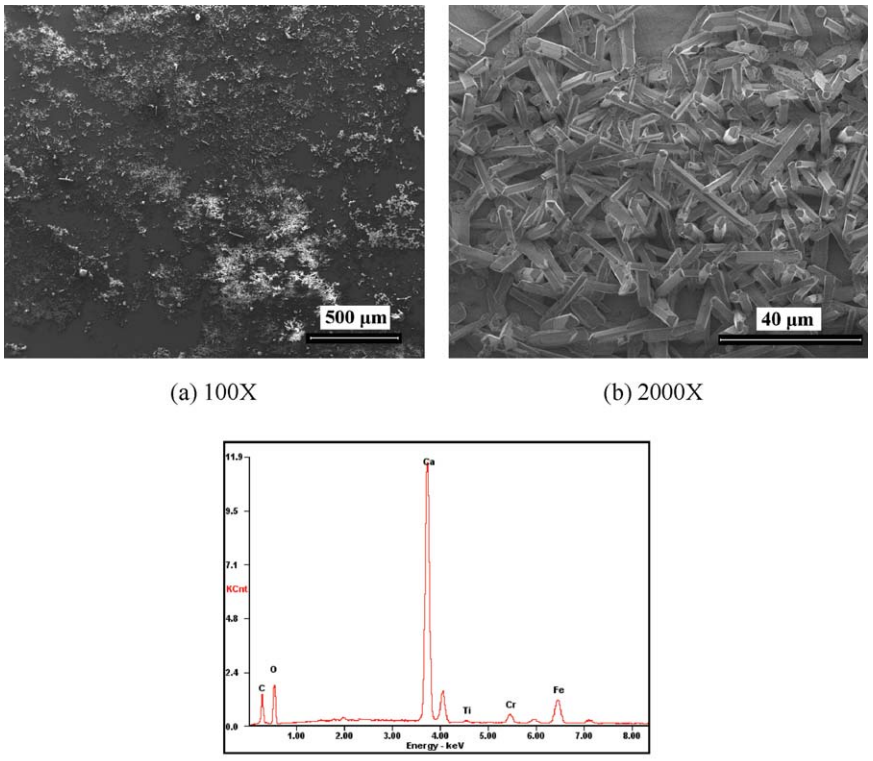

(a) 100X (b) 2000X

(c) Spectrum diagram and element content

Figure 14. FE-SEM and EDS analyses of fouling layer on coating C (1 μm=10^{-6} m).

(a) 100×; (b) 2000×; and (c) spectrum diagram and element content. [Color figure can be viewed in the online issue, which is available at wileyonlinelibrary.com.]

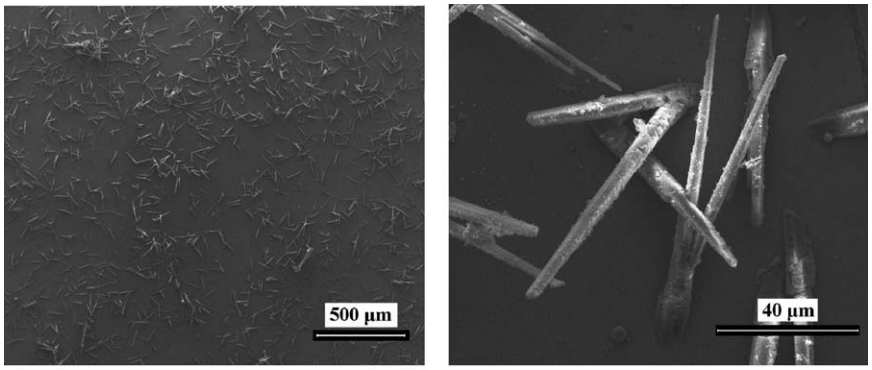

(a) 100X (b) 2000X

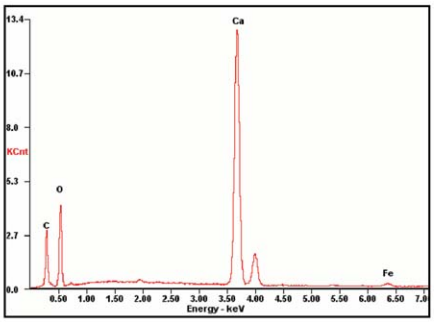

(c) Spectrum diagram and element content

Figure 15. FE-SEM and EDS analyses of fouling layer on coating CF (1 μm=10^{-6} m).

(a) 100×; (b) 2000×; and (c) spectrum diagram and element content. [Color figure can be viewed in the online issue, which is available at wileyonlinelibrary.com.]

foulant crystals deposited on the plate and the bottom of the pool in the fouling experiments due to the low solubility of $CaCO_3$.[27] The pH value of $CaCO_3$ solution was about 8.4 at the initial concentration of 0.25 kg m^{-3} and reached a constant value of 9.3, as shown in Figure 17.

Fouling in different heat fluxes of $CaCO_3$ solution

Figure 18 shows the variation of fouling resistance for different heat fluxes at initial $CaCO_3$ concentration of 0.25 kg m^{-3} on coating C. The experimental results show that the fouling resistance curves exhibit near the same trends, and the fouling resistance increases with the increase of heat flux. When heat flux increased, the number of the nucleate sites on heat-transfer surface increased, and more vapor bubbles generated on per unit area and the boiling bubble departure frequency also increased. Thus, the amount of the foulant increased at the bottom of the vapor bubbles. In addition, the surface temperature became high due to the high heat flux. Hence, the formation rate of $CaCO_3$ fouling became high and leaded to the increase of fouling resistance. It should be noted that the fluctuations of fouling resistance values at low heat flux of 33,470 W m^{-2} was relatively large, which may be caused by the instability of the supply voltage of the copper heater during the fouling experiment.

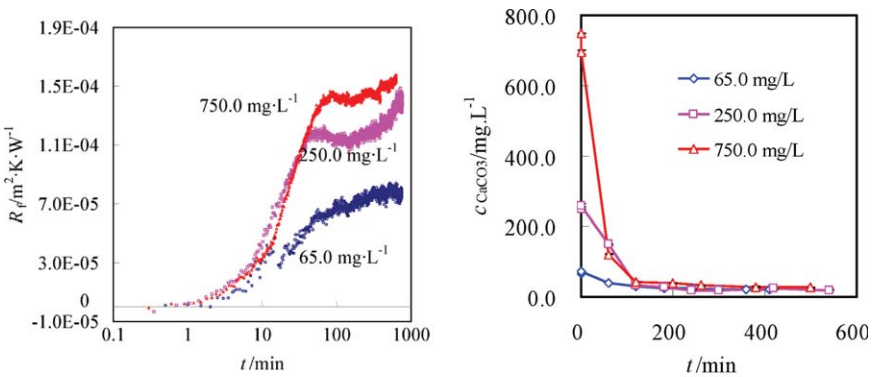

(a) R_f vs. t (b) c_{CaCO_3} vs. t

Figure 16. Fouling resistance and $CaCO_3$ concentration vs. time on coating C at heat flux of 50,690 W m^{-2} (1 mg L^{-1}=10^{-3} kg m^{-3}; 1 min=60 s).

(a) R_f vs. t and (b) c_{CaCO_3} vs. t. [Color figure can be viewed in the online issue, which is available at wileyonlinelibrary.com.]

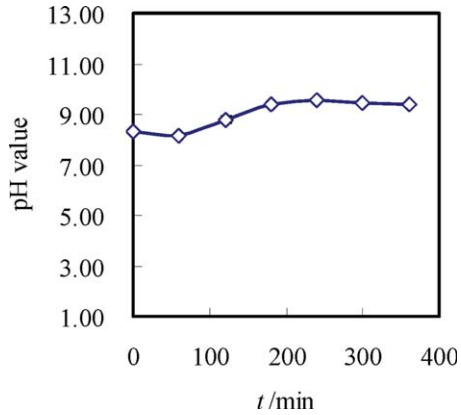

Figure 17. Solution pH value vs. fouling time at initial $CaCO_3$ concentration of 0.25 kg m^{-3} (1 min=60 s).

[Color figure can be viewed in the online issue, which is available at wileyonlinelibrary.com.]

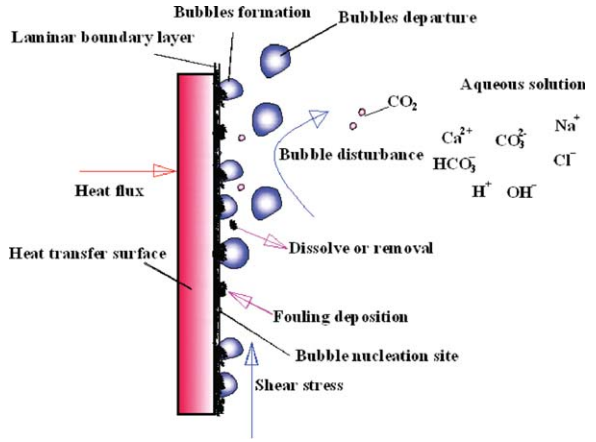

Figure 19. Schematic diagram of vapor bubbles formation, motion, fouling deposition, and removal on vertical surface in pool boiling.

[Color figure can be viewed in the online issue, which is available at wileyonlinelibrary.com.]

Fouling data modeling

Fouling formation on heat-transfer surface is jointly controlled by deposition and removal processes.[47] In the pool boiling, no forced bulk flow and fouling removal process is affected by the disturbance of vapor bubbles adjacent to the boiling surface. The schematic diagram to show the relationship between vapor bubbles dynamics and fouling formation and removal is shown in Figure 19.

As indicated in Figures 11, 16, and 18, the relationship between $CaCO_3$ fouling resistance and time basically shows an asymptotic tendency. Hence, the experimental data of $CaCO_3$ fouling resistance in this work are modeled with following equation[48]

$$R_f = R_f^{\infty}\left(1 - e^{-t/t_c}\right) \tag{3}$$

where R_f^{∞} is the asymptotic fouling resistance, and t_c is the time constant.

Parameters R_f^{∞} and t_c in Eq. 3 were determined from the experimental data by the nonlinear regression[48,49] of experimental data with Statistica v8.0 commercial software and shown in Table 4. Four modeled fouling curves compared with the experimental data are shown in Figure 20. As seen in Figure 20, the modeled fouling curves agree basically to the experimental ones with the maximum deviation of 7.06%, minimum deviation of 2.21%, and average deviation of 4.14%. The comparison results indicate that asymptotic fouling resistance model can describe the $CaCO_3$ fouling behavior in the pool boiling in the present conditions ($CaCO_3$ initial concentration: 0.065–0.75 kg m^{-3}, heat flux: 33,470–63,250 W m^{-2}). Predictive curve is higher than the experimental data at the early stage of the fouling tests, which is due to the existence of negative fouling resistances at the beginning of the fouling tests. Experimental fouling curve is not an ideal smooth one, which indicates that there are other factors (boiling pool pressure, flow rate of cooling water, etc.) that affect the measurement of the fouling resistance. Further work is needed to establish a mechanism fouling model from the point of view of microboiling mechanism.

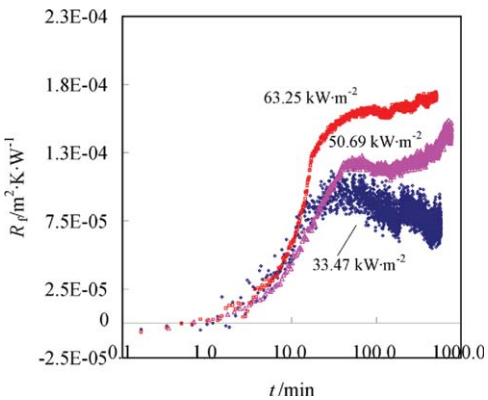

Figure 18. Effect of heat flux on fouling resistance at initial $CaCO_3$ concentration of 0.25 kg m^{-3}.

[Color figure can be viewed in the online issue, which is available at wileyonlinelibrary.com.]

Concluding Remarks

The density of nucleation sites and departure frequency of vapor bubbles on microscale–nanoscale hydrophobic TiO_2–FPS composite coatings in the pool boiling were far greater than those on TiO_2 coating as well as polished SS surfaces, and, thus, pool boiling enhancement on the TiO_2–FPS coatings of deionized water was observed. Meanwhile, heat-transfer deterioration on the dense and thick TiO_2 coatings and TiO_2–FPS coatings was also obtained. Asymptotic fouling resistance of $CaCO_3$ solution on the TiO_2–FPS coatings during pool boiling decreased obviously compared with the TiO_2 coatings, and the fouling on the TiO_2–FPS film surfaces was easy to remove. $CaCO_3$ crystalline form deposited

Table 4. Parameters of R_f^{∞} and t_c for Each Sample (1 min=60 s)

Sample	R_f^{∞} (m^2 kW^{-1})	t_c (min)
DF	1.115×10^{-4}	14.377
SS	1.678×10^{-4}	29.419
C	1.390×10^{-4}	20.626
CF	6.180×10^{-5}	18.927

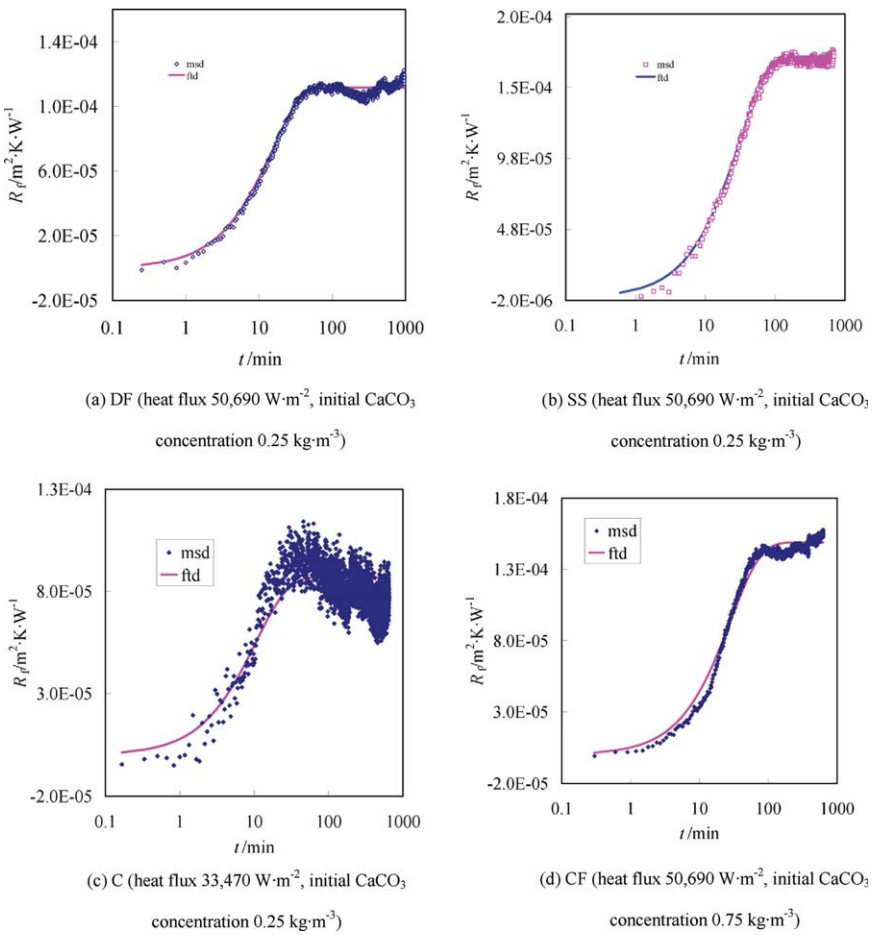

Figure 20. Comparisons of modeled and measured $CaCO_3$ fouling curves (msd, measured; ftd, modeled).

(a) DF (heat flux 50,690 W m^{-2}, initial $CaCO_3$ concentration 0.25 kg m^{-3}); (b) SS (heat flux 50,690 W m^{-2}, initial $CaCO_3$ concentration 0.25 kg m^{-3}); (c) C (heat flux 33,470 W m^{-2}, initial $CaCO_3$ concentration 0.25 kg m^{-3}); and (d) CF (heat flux 50,690 W m^{-2}, initial $CaCO_3$ concentration 0.75 kg m^{-3}). [Color figure can be viewed in the online issue, which is available at wileyonlinelibrary.com.]

on the TiO_2 coatings was calcite, whereas the polymorph accumulated on the TiO_2–FPS coatings was aragonite. There were more nucleation sites and more vapor bubbles in small size on the TiO_2–FPS coating surface than on the TiO_2 coating and polished SS surfaces. $CaCO_3$ crystals on unit area of the TiO_2–FPS coating surface were much less than on the other surfaces. The TiO_2–FPS coating exhibited a favorable pool boiling and antifouling performances. Asymptotic fouling model could be used to model the fouling resistances data in the pool boiling of $CaCO_3$ solution with good agreement. The comprehensive investigations of this article suggest a potential way to inhibit fouling as well as to improve pool boiling. Much work is needed to establish more fundamental fouling model on these coatings.

Acknowledgments

The authors are grateful to the National Natural Science Foundation of China (No. 20876106), National High Technology Research and Development Program 863(No.2012AA052804), and Tianjin Research Program of Application Foundation and Advanced Technology (No. 09JCZDJC24100) for the financial support. The authors thank Prof. Yang and Dr. Cao for their very valuable suggestions on the establishment of the pool boiling apparatus. The authors thank Prof. Tan for her help in the numerical simulations of distribution of heat flux. The authors also thank Mr. Xu and Mr. Zhou for their help of the boiling bubbles video capture tests.

Notation

at = atom percentage, %
c = concentration, mg L^{-1} (kg m^{-3})
c = Constant
D = diameter of vapor bubble or copper plate, m
E = activation energy, J mol^{-1}
F = departure frequency of vapor bubble from heat-transfer surface, Hz
I = electric current, A
$\dot{q}$ = heat flux, W m^{-2}
R_a = arithmetical mean deviation of profile, m
R = fouling resistance, m^2 K W^{-1}
T = temperature, K
T = time, s
U = voltage, V

Greek letters

α = heat-transfer coefficient, W m^{-2} K^{-1}
Γ = surface free energy, J m^{-2}
δT = temperature difference, K
θ = contact angle,°
I, II, III, IV = valence of Ti element

Abbreviations

AES = auger electron spectroscopy
B, C, D = TiO_2 coatings with different thicknesses

BF, CF, DF = titania–fluoroalkylsilane coatings based on the B, C and D coatings
DLC = diamond-like carbon
EDS = energy dispersive X-ray spectroscopy
FE-SEM = field emission scanning microscopy
FPS = fluoroalkylsilane
LPD = liquid-phase deposition
SS = AISI304 stainless steel
XDLVO = extended DLVO theory
XPS = X-ray photoelectron spectroscopy

Superscripts and subscripts

0 = initial
* = equilibrium
+ = electron-acceptor component
− = electron-acceptor component
AB = Lewis acid–base component
b = bulk, bubble, or binding
c = time constant
d = departure, deposited, or diiodomethane
f = fouled or formamide
g = growth
LW = nonpolar component
s = surface
t = time
w = waiting time, water, or wall
∞ = final state of fouling resistance

Literature Cited

1. Taborek J, Aoki T, Ritter RB, Palen JW, Knudsen JG. Fouling: the major unresolved problem in heat transfer. *Chem Eng Prog*. 1972;68(2):59–67.
2. Yang SR, Xu ZM, Sun LF. Heat Exchanger Fouling and Strategies, 2nd ed. Beijing: Science Press, 2004.
3. Malayeri MR, Al-Janabi A, Müller-Steinhagen H. Application of nano-modified surfaces for fouling mitigation. *Int J Energy Res*. 2009;33(13):1101–1113.
4. Yang QF, Liu YQ, Gu AZ, Ding J, Shen ZQ. Investigation of induction period and morphology of $CaCO_3$ fouling on heated surface. *Chem Eng Sci*. 2002;57(6):921–931.
5. Bott TR. Fouling control and energy conservation. In: Thermal Issues in Emerging Technologies. Cairo, Egypt: IEEE, 2007:191–198.
6. Helalizadeh A, Müller-Steinhagen H, Jamialahmadi M. Mixed salt crystallisation fouling. *Chem Eng Process*. 2000;39(1):29–43.
7. Steinhagen R, Müller-Steinhagen H, Maani K. Problems and costs due to heat exchanger fouling in New Zealand industries. *Heat Transfer Eng*. 1993;14(1):19–30.
8. Geddert T, Bialuch I, Augustin W, Scholl S. Extending the induction period of crystallization fouling through surface coating. *Heat Transfer Eng. 2009-04-10* 2009;30(10–11):868–875.
9. Müller-Steinhagen H, Branch CA. Heat transfer and heat transfer fouling in Kraft black liquor evaporators. *Exp Therm Fluid Sci*. 1997;14(4):425–437.
10. Zettler HU, Wei M, Zhao Q, Müller-Steinhagen H. Influence of surface properties and characteristics on fouling in plate heat exchangers. *Heat Transfer Eng*. 2005;26(2):3–17.
11. Rosmaninho R, Melo LF. Calcium phosphate deposition from simulated milk ultrafiltrate on different stainless steel-based surfaces. *Int Dairy J*. 2006;16(1):81–87.
12. Zhao Q, Liu Y. Investigation of graded Ni-Cu-P-PTFE composite coatings with antiscaling properties. *Appl Surf Sci*. 2004;229(1–4):56–62.
13. Rosmaninho R, Rocha F, Rizzo G, Müller-Steinhagen H, Melo LF. Calcium phosphate fouling on TiN-coated stainless steel surfaces: role of ions and particles. *Chem Eng Sci*. 2007;62(14):3821–3831.
14. Förster M, Bohnet M. Modification of molecular interactions at the interface crystal/heat transfer surface to minimize heat exchanger fouling. *Int J Therm Sci*. 2000;39(7):697–708.
15. Jamialahmadi M, Müller-Steinhagen H. Scale formation during nucleate boiling—a review. *Corros Rev*. 1993;11(1–2):26–54.
16. Zhao Q, Liu Y, Wang C, Wang S, Müller-Steinhagen H. Effect of surface free energy on the adhesion of biofouling and crystalline fouling. *Chem Eng Sci*. 2005;60(17):4858–4865.
17. Zhao Q, Wang X. Heat transfer surfaces coated with fluorinated diamond-like carbon films to minimize scale formation. *Surf Coat Technol*. 2005;192(1):77–80.
18. Liu MY, Wang H, Wang Y. Enhancing flow boiling and antifouling with nanometer titanium dioxide coating surfaces. *AIChE J*. 2007;53(5):1075–1085.
19. Wang LL, Liu MY. Pool boiling fouling and corrosion properties on liquid-phase-deposition TiO_2 coatings with copper substrate. *AIChE J*. 2011;57(7):1710–1718.
20. Lai YK, Gao XF, Zhuang HF, Huang JY, Lin CJ, Jiang L. Designing superhydrophobic porous nanostructures with tunable water adhesion. *Adv Mater*. 2009;21(37):3799–3803.
21. Takata Y, Hidaka S, Uraguchi T. Boiling feature on a super water-repellent surface. *Heat Transfer Eng*. 2006;27(8):25–30.
22. Cai Y, Liu M. Corrosion behavior of titania films coated by liquid-phase deposition on AISI304 SS substrates. *AIChE J*. 2012;58(6):1907–1920.
23. Michalski MC, Hardy J, Saramago BJV. On the surface free energy of PVC/EVA polymer blends: comparison of different calculation methods. *J Colloid Interface Sci*. 1998;208(1):319–328.
24. Van Oss CJ, Chaudhury MK, Good RJ. Interfacial Lifshitz-van der Waals and polar interactions in macroscopic systems. *Chem Rev*. 1988;88(6):927–941.
25. Kim WT, Cho YI. A study of scale formation around air bubble attached on a heat-transfer surface. *Int Commun Heat Mass Transfer*. 2002;29(1):1–14.
26. People's Republic of China International Quality Supervision IAQ. Industrial circulating cooling water—determination of calcium and magnesium–EDTA titration method. GB/T 15452-2009. Beijing: China Standard Press, 2009:1–2.
27. Najibi SH, Müller-Steinhagen H, Jamialahmadi M. Calcium carbonate scale formation during subcooled flow boiling. *J Heat Transfer*. 1997;119(4):767–775.
28. Hozumi A, Ushiyama K, Sugimura H, Takai O. Fluoroalkylsilane monolayers formed by chemical vapor surface modification on hydroxylated oxide surfaces. *Langmuir*. 1999;15(22):7600–7604.
29. Pouilleau J, Devilliers D, Groult H, Marcus P. Surface study of a titanium-based ceramic electrode material by X-ray photoelectron spectroscopy. *J Mater Sci*. 1997;32(21):5645–5651.
30. Yu JG, Zhao XJ, Zhao QN, Du JC. XPS of study of TiO_2 photocatalytic thin film prepared by the sol–gel method. *Chin J Mater Res*. 2000;14:203–209.
31. Takata Y, Hidaka S, Cao JM, Nakamura T, Yamamoto H, Masuda M, Ito T. Effect of surface wettability on boiling and evaporation. *Energy*. 2005;30(2–4):209–220.
32. Takata Y, Hidaka S, Masuda M, Ito T. Pool boiling on a superhydrophilic surface. *Int J Energy Res*. 2003;27(2):111–119.
33. Takata Y. Surface wettability effects in heat and fluid flow. In: ASME 4th International Conference on Nanochannels, Microchannels, and Minichannels. Limerick, Ireland, 2006.
34. Wasserman SR, Tao YT, Whitesides GM. Structure and reactivity of alkylsiloxane monolayers formed by reaction of alkyltrichlorosilanes on silicon substrates. *Langmuir*. 1989;5(4):1074–1087.
35. Wasserman SR, Whitesides GM, Tidswell IM, Ocko BM, Pershan PS, Axe JD. The structure of self-assembled monolayers of alkylsiloxanes on silicon: a comparison of results from ellipsometry and low-angle X-ray reflectivity. *J Am Chem Soc*. 1989;111(15):5852–5861.
36. Zhang QH, Gao L, Lin XH. Shanghai Institute of Ceramics, Chinese Academy of Sciences. A method to form hydrophobic transparent films in the surface of a variety of substrates. China patent ZL 200610116543.5. September 27, 2006.
37. Liu GQ, Ma LX, Liu J, editors. Handbook of Chemistry and Chemical Property data (Inorganic Volume). Beijing: Chemical Industry Press, 2002.
38. Chu H, Yu B. A new comprehensive model for nucleate pool boiling heat transfer of pure liquid at low to high heat fluxes including CHF. *Int J Heat Mass Transfer*. 2009;52(19–20):4203–4210.
39. Wang CH, Dhir VK. Effect of surface wettability on active nucleation site density during pool boiling of water on a vertical surface. *J Heat Transfer*. 1993;115(3):659–669.
40. Pioro IL, Rohsenow WM, Doerffer SS. Nucleate pool-boiling heat transfer. I. Review of parametric effects of boiling surface. *Int J Heat Mass Transfer*. 2004;47(23):5033–5044.
41. Rankin BH, Adamson WL. Scale formation as related to evaporator surface conditions. *Desalination*. 1973;13(1):63–87.

42. Johnson MA, De La Peña J, Mesler RB. Bubble shapes in nucleate boiling. *AIChE J*. 1966;12(2):344–348.
43. Tang QG, Meng JP, Liang JS, Nie L, Li YX. Effects of copper based alloys on the nucleation and growth of calcium carbonate scale. *J Alloys Compd*. 2010;491(1–2):242–247.
44. Turner CW, Smith DW. Calcium carbonate scaling kinetics determined from radiotracer experiments with calcium-47. *Ind Eng Chem Res*. 1998;37(2):439–448.
45. Pääkkönen TM, Riihimäki M, Puhakka E, Muurinen E, Simonson CJ, Keiski RL. Crystallization fouling of $CaCO_3$—effect of bulk precipitation on mass deposition on the heat transfer surface. In: Paper presented at Proceedings of International Conference on Heat Exchanger Fouling and Cleaning VIII, Schladming, Austria, 2009.
46. Esawy M, Abd-Elhady MS, Malayeri MR, Müller-Steinhagen H. Influence of sintering on deposit formation during pool boiling of calcium sulphate solutions. *Exp Therm Fluid Sci*. 2010;34(8):1439–1447.
47. Bansal B, Chen XD, Müller-Steinhagen H. Deposition and removal mechanisms during calcium sulphate fouling in heat exchangers. *Int J Transport Phenomena*. 2005;7(1):1–22.
48. Bohnet M. Fouling of heat transfer surfaces. *Chem Eng Technol*. 1987;10(1):113–125.
49. Mwaba MG, Golriz MR, Gu J. A semi-empirical correlation for crystallization fouling on heat exchange surfaces. *Appl Therm Eng*. 2006;26(4):440–447.

Appendix: Details of Experiments and Measurements

The details of the electric heating unit are shown in Figure A1. The side surface of the copper rod was surrounded closely with an electric heating hoop. Three E-type thermocouples were fitted equidistantly along the axial central line of the copper rod. One of the thermocouples connected to the temperature controller to cut off the heating power if the internal temperature of the heater exceeded the temperature limitation. Two E-type thermocouples were located in different positions of the solution to measure the bulk temperature. Twelve bolts were used to install the test plate on the flange of the heating unit. A heat-resistant silicone gasket was used to ensure the solution did not discharge from the edge of the plate.

To measure the temperature of the pool boiling surface, three pairs of parallel holes were drilled in the plate (also see Figure A2). Both the temperatures in the center and on the surface of the plate were measured. The temperature difference between the center and the surface of the plate was obtained, and then a correlation curve between temperature difference and corresponding heat flux was plotted. Thus, the temperature

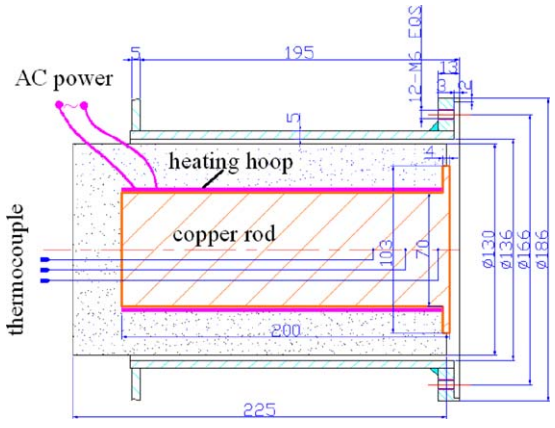

Figure A1. Electric heating unit.

[Color figure can be viewed in the online issue, which is available at wileyonlinelibrary.com.]

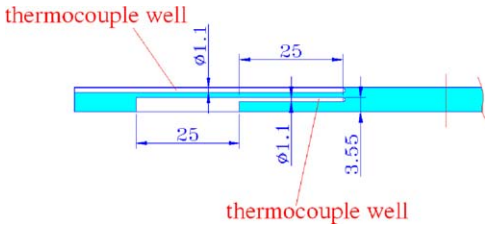

Figure A2. Temperature holes in the plate (unit: 10^{-3} m).

[Color figure can be viewed in the online issue, which is available at wileyonlinelibrary.com.]

on the heat-transfer surface was estimated by measuring three center temperatures of the plate for subsequent pool boiling and the fouling experiments. The formula for calculation of the surface temperature is shown in Eq. A1.

$$\bar{T}_{\mathrm{w}} = \frac{1}{3}\sum_{i=1}^{3}\left(T_{\mathrm{w,c}} - \delta T\right) \tag{A1}$$

where $\bar{T}_{\mathrm{w,c}}$ is the center temperature of the plate, and δT is the temperature difference between the center and the surface of the plate. The relationship between the temperature difference and heat flux is shown in Figure A3.

The heat flux distribution along the radial and axial directions within the plate (see Figure A4) was numerically calculated with ANSYS V14.0 software (ANSYS). The fluid contacted the plate was set to deionized water with temperature of 373 K. Boundary conditions are shown in Figure A5. Boundary a was set to boiling; b was convection; c–g were adiabatic; and f was constant heat flux, which was calculated based on the input current, voltage, and copper diameter of 0.07 m. Twenty-one local heat fluxes were used for the calculations. Boundaries of h and i were set to the axes of symmetry. As mentioned earlier, the materials of the electric heating unit and the plate are of copper and SS, respectively. Thermal conductivity and other properties of the materials were selected from the self-contained database of ANSYS software. The operation processes of meshes, boundary conditions, material settings, and numerical solving were carried out with "ANSYS mechanical of APDL module." The

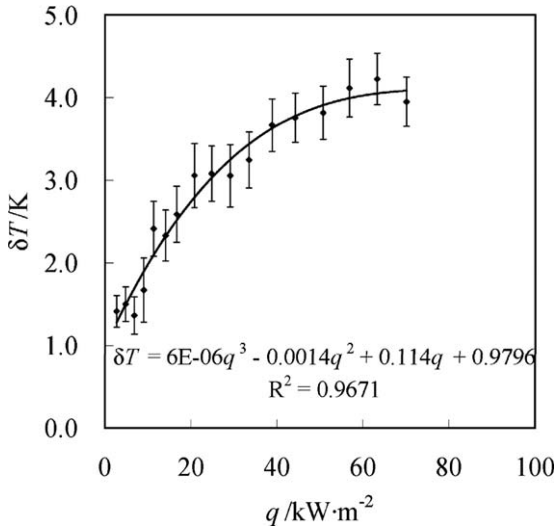

Figure A3. Temperature difference between surface and centre of the plate vs. heat flux.

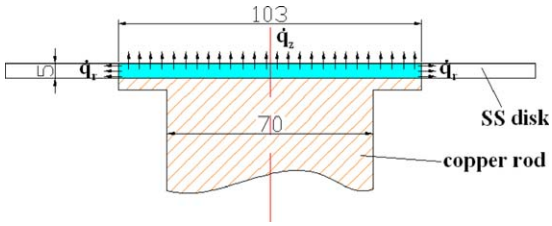

Figure A4. Heat flux distribution in the plate (unit: 10^{-3} m).

[Color figure can be viewed in the online issue, which is available at wileyonlinelibrary.com.]

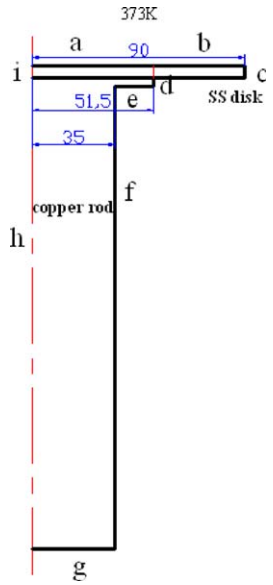

Figure A5. Boundary parameters setting of the numerical calculation (unit: 10^{-3} m).

[Color figure can be viewed in the online issue, which is available at wileyonlinelibrary.com.]

distributions of heat fluxes and temperatures in the copper rod and the plate were obtained. Typical simulation results of the heat flux in the copper rod and the plate are shown in Figure A6. Figure A7 shows the detailed distributions of the nodes. The results showed that the majority of the heat flowed in the axial direction of the plate. The proportion of the heat along the axial direction to the total is 90.2% and remains almost constant for different heat flow rates. Thus, the heat flux through the axial direction was calculated with the product of electric current I, voltage U, and divided by the contact area between copper rod and plate, and then multiplied by the factor of 0.902. The formula is shown in Eq. A1.

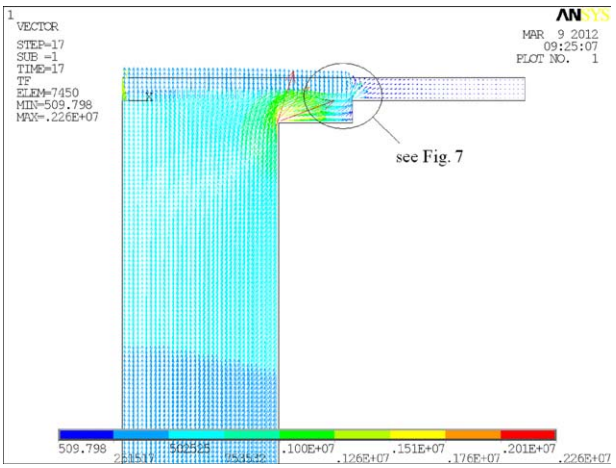

Figure A6. Distributions of heat fluxes simulated with ANSYS software in the plate and copper rod.

[Color figure can be viewed in the online issue, which is available at wileyonlinelibrary.com.]

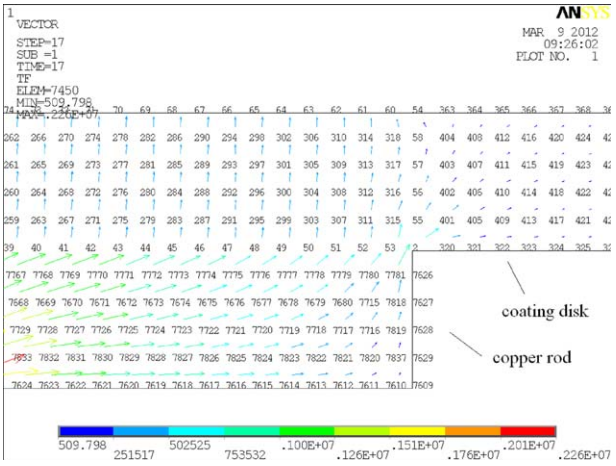

Figure A7. Distributions of the nodes and heat fluxes with ANSYS software.

[Color figure can be viewed in the online issue, which is available at wileyonlinelibrary.com.]

$$\dot{q} = \frac{U \cdot I}{\pi\left(D/2\right)^2 \times 90.2\%} \tag{A2}$$

where $\dot{q}$ is heat flux, I electric current, U voltage, and D contact diameter between copper rod and plate.

Manuscript received July 11, 2012, and revision received Nov. 3, 2012.